

Multicolor Super-Resolution Imaging with Photo-Switchable Fluorescent Probes

Mark Bates,¹ Bo Huang,^{2,3} Graham T. Dempsey,⁴ Xiaowei Zhuang^{2,3,5*}

Recent advances in far-field optical nanoscopy have enabled fluorescence imaging with a spatial resolution of 20 to 50 nanometers. Multicolor super-resolution imaging, however, remains a challenging task. Here, we introduce a family of photo-switchable fluorescent probes and demonstrate multicolor stochastic optical reconstruction microscopy (STORM). Each probe consists of a photo-switchable “reporter” fluorophore that can be cycled between fluorescent and dark states, and an “activator” that facilitates photo-activation of the reporter. Combinatorial pairing of reporters and activators allows the creation of probes with many distinct colors. Iterative, color-specific activation of sparse subsets of these probes allows their localization with nanometer accuracy, enabling the construction of a super-resolution STORM image. Using this approach, we demonstrate multicolor imaging of DNA model samples and mammalian cells with 20- to 30-nanometer resolution. This technique will facilitate direct visualization of molecular interactions at the nanometer scale.

As one of the most versatile imaging modalities in biology, fluorescence microscopy allows noninvasive imaging of cells and tissues with molecular specificity. The availability of fluorescent probes in many colors and the ability to label specific gene products enable visualization of molecular interactions in biological samples. However, the spatial resolution of optical microscopy, classically limited by the diffraction of light to ~300 nm, is inconveniently situated one to two orders of magnitude above the typical molecular length scales in cells. Various “super-resolution” optical imaging techniques have been developed to overcome this limit (1, 2). Among these methods, stimulated emission depletion microscopy (STED) and reversible saturable optically linear fluorescence transition (RESOLFT) techniques (2, 3), saturated structured illumination microscopy (SSIM) (4), stochastic optical reconstruction microscopy (STORM) (5), and photoactivated localization microscopy (PALM) (6, 7) have achieved 20- to 50-nm resolution in the far field and promise to preserve the inherent noninvasive imaging capability of optical microscopy. In certain cases, binding kinetics or translational motions of individual molecules have also been used to map out high-resolution structures in cells (8–10).

Nonetheless, multicolor super-resolution imaging remains a difficult task, leaving many biological questions beyond the reach of optical

methods. Among the various multicolor imaging techniques, fluorescence resonance energy transfer (FRET) is particularly powerful for probing molecular interactions on the nanometer scale (11–14), although it is difficult to determine the precise locations and organizations of molecules from a FRET image. Fluorescence colocalization offers another approach to detect molecular interactions, but has traditionally been used within the boundaries of diffraction-limited imaging and would benefit from a combination with super-resolution techniques (15). Here, we report a family of photo-switchable probes with distinct colors and demonstrate multicolor STORM imaging with 20- to 30-nm resolution.

STORM relies on the detection of single fluorescent molecules (16) and the localization of these molecules with nanometer accuracy (17–21). Limited only by the number of photons detected (17), localization accuracies as high as 0.1 to 1 nm can be achieved for bright fluorescent or scattering objects (22–25). By using photo-switchable probes, one can modulate the fluorescence emission profile of individual fluorophores in time such that only an optically resolvable subset of fluorophores are activated at any moment, allowing their localization with high accuracy. Over the course of multiple activation cycles, the positions of numerous fluorophores are determined and used to construct a high-resolution STORM image (5–7). The development of multicolor STORM thus depends on the construction of bright, photo-switchable probes with distinct colors.

To search for chromatically distinguishable photo-switchable probes, we turned to cyanine dyes with various lengths of polymethine chains (fig. S1) (26–28). We constructed a series of dye pairs, each consisting of a cyanine dye and a shorter-wavelength chromophore, as inspired by our earlier work on photo-switchable Cy5 (27). These dye pairs were conjugated to double-

stranded DNA or antibody and immobilized on microscope slides for single-molecule detection (26). A series of cyanine dyes with distinct absorption and emission spectra displayed robust photo-switching behavior when paired with a Cy3 molecule in close proximity (fig. S1) (26). Figure 1A shows fluorescence time traces obtained from single molecules of Cy5, Cy5.5, and Cy7 as they undergo multiple switching cycles. Upon illumination with a red laser (657 nm), each of the three dyes was initially fluorescent and then quickly switched into a nonfluorescent, dark state. A brief exposure to a green laser pulse (532 nm) led to reactivation of the dyes back to the fluorescent state. Without a proximal Cy3, the reactivation of Cy5, Cy5.5, or Cy7 was barely detectable under our excitation conditions. We therefore refer to the Cy3 dye as the “activator” and Cy5, Cy5.5, or Cy7 as the photo-switchable “reporter.” These reporters typically can be switched on and off for hundreds of cycles before permanently photobleaching.

The rate constant of switching from the fluorescent to the dark state, designated k_{off} , scaled linearly with the red laser power (Fig. 1B). Consistent with this observation, the average number of photons detected per switching cycle was a constant, independent of the laser power. The number of photons detected was ~3000 for Cy5 and Cy5.5 and ~500 for Cy7 under prism-type total internal reflection fluorescence (TIRF) imaging geometry, and these numbers doubled under objective-type TIRF imaging geometry (26). The activation rate, k_{on} , from the dark to the fluorescent state, was linear with respect to the green laser power (Fig. 1B). The linear dependence of both rate constants extended over the entire range of laser powers tested, suggesting that faster switching rates are possible at higher laser intensities. As shown previously, their distinct emission spectra (fig. S1) allow Cy5, Cy5.5, and Cy7 to be distinguished at the single-molecule level (29), suggesting one approach to accomplish multicolor STORM imaging.

The above results indicate that chromatically distinguishable photo-switchable reporters can be activated by the same activator dye. As a further exploration, we tested whether other dyes with distinct spectral properties can be used as activators. To this end, Cy3, Cy2, and Alexa Fluor 405 (fig. S1) (26) were paired with Cy5. Switching traces for individual pairs are shown in Fig. 1C. Again, Cy5 was quickly switched into the dark state upon illumination with a red laser. The activation of Cy5, however, required different-colored lasers corresponding to the absorption wavelengths of the activators. The Alexa 405-Cy5 pair was efficiently activated by a violet laser (405 nm), but was much less sensitive to blue (457 nm) and green (532 nm) activation light. Similarly, the Cy2-Cy5 pair and Cy3-Cy5 pair were most sensitive to the blue and green lasers, respectively. To determine the activation specificity quantitatively, we measured the activation rate constants for these dye pairs at the

¹School of Engineering and Applied Sciences, Harvard University, Cambridge, MA 02138, USA. ²Howard Hughes Medical Institute, Harvard University, Cambridge, MA 02138, USA. ³Department of Chemistry and Chemical Biology, Harvard University, Cambridge, MA 02138, USA. ⁴Graduate Program in Biophysics, Harvard University, Cambridge, MA 02138, USA. ⁵Department of Physics, Harvard University, Cambridge, MA 02138, USA.

*To whom correspondence should be addressed. E-mail: zhuang@chemistry.harvard.edu

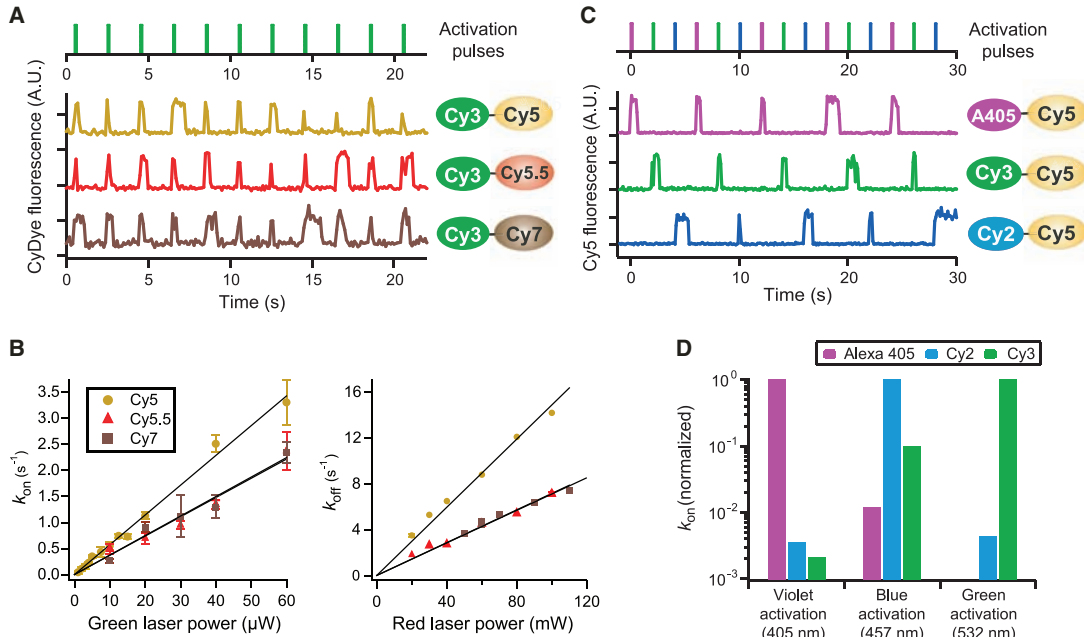
three wavelengths: 405, 457, and 532 nm. For each wavelength, the pair with the appropriate activator was activated rapidly, with a rate at least 10 times as high as those measured for the other

two pairs (Fig. 1D), indicating high activation specificity.

This selective activation provides a second parameter for multicolor detection. Not only can

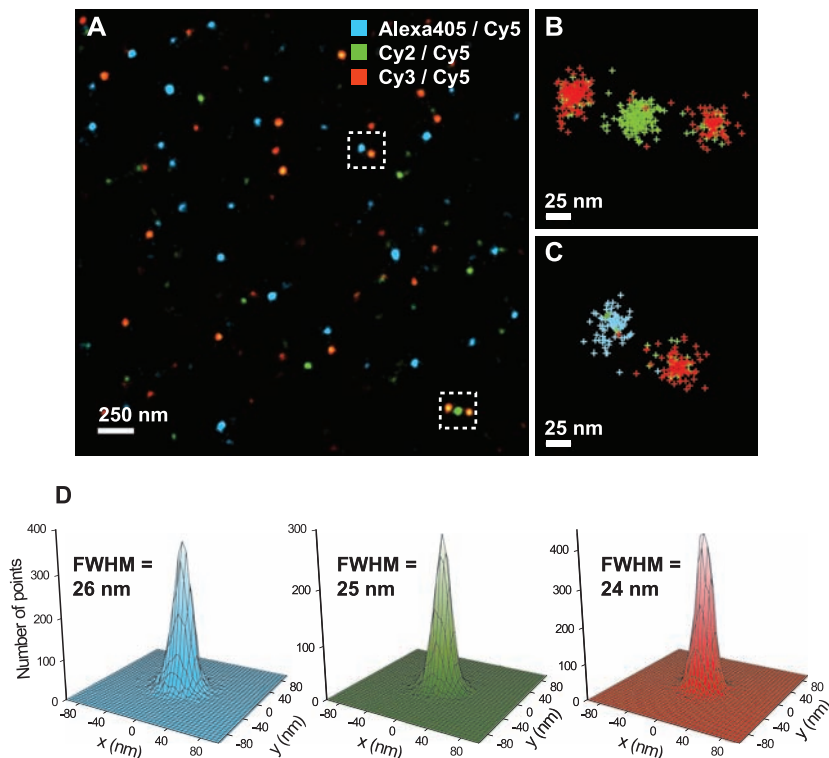
different activator-reporter pairs be distinguished by their emission color, as determined by the reporter dye, but they can also be differentiated by the color of light which activates them, as

Fig. 1. Photo-switchable probes constructed from activator-reporter pairs. **(A)** Spectrally distinct reporters exhibit photo-switching behavior. The lower panel shows the fluorescence time traces of three photo-switchable reporters Cy5 (dark yellow line), Cy5.5 (red line), and Cy7 (brown line), each paired with a Cy3 dye as the activator on a DNA construct. The upper panel shows the green laser pulses (532 nm) used to activate the reporters. The red laser (657 nm) was continuously on, serving to excite fluorescence from the reporters and to switch them to the dark state. Traces were shifted relative to each other for clarity. **(B)** Switching rate constants k_{on} and k_{off} of the Cy3-Cy5, Cy3-Cy5.5, and Cy3-Cy7 pairs as a function of green and red laser power. Error bars indicate SEM from about three data sets. The laser power to intensity calibration may vary between different samples because of moderate differences in the laser spot size at the sample. **(C)** The same reporter can be activated by spectrally distinct activators. The lower panel shows the fluorescence time traces of Cy5 paired with three different activators, Alexa 405 (magenta line), Cy2 (blue line), and Cy3 (green line). The upper panel shows the violet (405 nm, magenta line), blue (457 nm, blue line), and green (532 nm, green line) activation pulses. **(D)**



Normalized activation rate constants of the three dye pairs at three activation wavelengths: 405, 457, and 532 nm. The k_{on} values of Alexa 405-Cy5, Cy2-Cy5, and Cy3-Cy5 were used for normalization at 405, 457, and 532 nm, respectively. The absolute activation rates were rapid for each pair at its corresponding optimal wavelength, with values of 10 s^{-1} or greater at only a few hundred μW of laser power. The activation rate of the Alexa 405-Cy5 pair by the 532-nm laser was too small to be measured reliably.

Fig. 2. Three-color STORM imaging of a model DNA sample. **(A)** Three-color STORM image of three different DNA constructs labeled with Alexa 405-Cy5, Cy2-Cy5, or Cy3-Cy5 mixed at a high surface density on a microscope slide. The image was plotted by rendering each localization as a Gaussian peak, the width of which was scaled with the theoretical localization accuracy given by the number of photons detected (26). Each colored spot in this image represents a cluster of localizations from a single DNA molecule. A conventional fluorescence image of the same area is shown in fig. S3 for comparison. **(B and C)** Higher-magnification views of the boxed regions in (A) show several examples of closely spaced DNA molecules. Each localization was plotted as a cross, colored according to the following code: If the molecule was activated by a 405-, 457-, or 532-nm laser pulse, the color of the cross was assigned as blue, green, or red, respectively. **(D)** The localization distributions of the blue, green, or red clusters. The two-dimensional histograms of localizations were generated by aligning multiple (50 to 60) clusters by their center of mass. The histograms were fit to a Gaussian profile to determine their FWHM.



determined by the activator dye. A combinatorial pairing of the three reporters and three activators reported here could generate up to nine distinguishable fluorescent probes, but requires only four light sources for excitation and three spectrally distinct channels for detection. Photo-switching appeared not to be limited by the spectral separation between the dyes, as illustrated by efficient activation of Cy7 by Alexa 405 (fig. S2), even though the two dyes lie at opposite extremes of the visible spectrum with absorption maxima ~ 350 nm apart (fig. S1) (26). We expect this combinatorial scheme to substantially expand multicolor imaging capabilities at both conventional and subdiffraction limit resolutions.

Here, we use the selective activation scheme as an initial demonstration of multicolor STORM imaging. Three different DNA constructs labeled with Alexa 405-Cy5, Cy2-Cy5, or Cy3-Cy5 were mixed and immobilized on a microscope slide at a high surface density such that individual DNA molecules could not be resolved in a conventional fluorescence image (fig. S3) (26). To generate a STORM image, the sample was first exposed to a red laser (633 nm) to switch off nearly all Cy5 dyes in the field of view. The sample was then periodically excited with a sequence of violet (405 nm), blue (457 nm), and green (532 nm) laser pulses, each of which activated a sparse, optically resolvable subset of fluorophores. In between activation pulses, the sample was imaged with the red laser. The image of each activated fluorescent spot was analyzed to determine its centroid position (referred to as a localization), and a color was assigned according to the preceding activation pulse. Because the same imaging laser and detection channel were used for all three dye pairs, there was no need for correction of chromatic aberration. After thousands of activation cycles, a STORM image was constructed by plotting all of the colored localizations (Fig. 2, A to C). In contrast to the conventional image (fig. S3), the STORM image showed clearly separated clusters of localizations, each cluster corresponding to an individual DNA molecule and resulting from repetitive localizations of a single Cy5 molecule over multiple switching cycles. Most of the localizations within each cluster displayed the same color, identifying the type of activator dye present on the DNA and illustrating multicolor imaging capability through selective activation. We identified two origins of crosstalk between colors: false activation by laser pulses of incorrect colors (for example, activation of the Cy3-Cy5 pair by blue pulses) and nonspecific activation by the red imaging laser (26). Both effects were quantitatively small (fig. S4) (26). The localizations within each cluster approximately follow a Gaussian distribution with a full width at half maximum (FWHM) of 26 ± 1 nm, 25 ± 1 nm, and 24 ± 1 nm for the Alexa 405, Cy2, and Cy3 clusters, respectively (Fig. 2D), suggesting an imaging resolution of ~ 25 nm for three-color STORM imaging. This resolution is lower than the theoretical limit

predicted from the number of photons detected (26), likely due to the residual stage drift that was not completely accounted for by the drift correction.

Applying STORM to cell imaging, we first performed single-color immunofluorescence imaging of microtubules, filamentous cytoskeleton structures important for many cellular functions. BS-C-1 cells were immunostained with primary antibodies and then with activator-reporter-labeled secondary antibodies (26). Cy3 was used as the activator and Alexa Fluor 647, a cyanine dye with structural, spectral, and photo-switching properties very similar to those of Cy5, was used as the reporter (fig. S1). The STORM image shows a drastic improvement in the resolution of the microtubule network as compared to the conventional fluorescence image (Fig. 3, A to F). In the regions where microtubules were densely packed and undefined in the conventional image, individual microtubule filaments were

clearly resolved by STORM (Fig. 3, C to F). For example, two filaments 80 nm apart appeared well separated in the STORM image (Fig. 3G). Whole-cell STORM images, including $\sim 10^6$ single-molecule localizations, were acquired in 2 to 30 min, an improvement of one to two orders of magnitude over the previously reported imaging speed of PALM (6). Super-resolution microtubule structures began to emerge after only 10 to 20 s of STORM imaging.

To determine the imaging resolution more quantitatively, we identified pointlike objects in the cell, appearing as small clusters of localizations away from any discernable microtubule filaments. These clusters likely represent individual antibodies nonspecifically attached to the cell. The width (FWHM) of the localization clusters was 24 ± 1 nm (fig. S5) (26), giving a measure of the image resolution inside the cell. Next, we measured the apparent width of an individual microtubule filament in the STORM

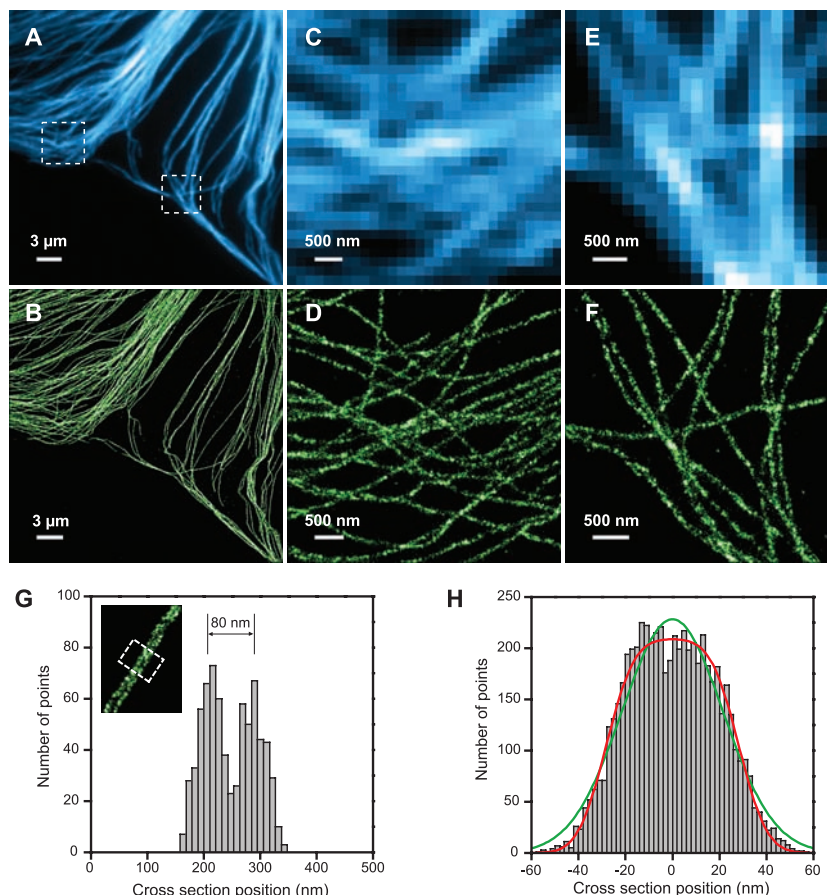


Fig. 3. STORM imaging of microtubules in a mammalian cell. (A) Conventional immunofluorescence image of microtubules in a large area of a BS-C-1 cell. (B) STORM image of the same area. (C and E) Conventional and (D and F) STORM images corresponding to the boxed regions in (A). (G) Cross-sectional profiles of two nearby microtubule filaments in the cell. The inset shows the STORM image, and the histogram shows the cross-sectional distribution of localizations within the small regions specified by the white box. (H) Cross-sectional profile of a microtubule segment determined from the STORM image. A relatively long segment (~ 7 μm) was chosen to obtain good statistics. The histogram shows the cross-sectional distribution of localizations. The green line is a single Gaussian fit with FWHM = 51 nm. The red line shows the fit obtained by convolving a rectangular function of width = d with a Gaussian function of FWHM = r . The fit yields $d = 56$ nm and $r = 22$ nm, corresponding to the antibody-coated microtubule width and the imaging resolution, respectively.

image by examining its cross-sectional profile. Figure 3H shows a cross-sectional distribution of localizations for a microtubule segment. A simple Gaussian fit to the profile yielded a FWHM of 51 nm but deviates significantly from the actual distribution, which appeared flat-topped presumably due to the finite width of the microtubule. A better fit was obtained by simulating the actual microtubule cross-section as a rectangular function of width d , but convolving it with a Gaussian function with FWHM r to model our image resolution. From the fit, we obtained an intrinsic imaging resolution of $r = 22$ nm, consistent with the localization accuracy determined from the pointlike objects. The microtubule width derived from the fit, $d = 56$ nm, is in agreement with the 60-nm width of antibody-stained microtubules previously determined by electron microscopy (30). However, this apparent width is significantly larger than the diameter of a bare

microtubule without antibody coating, pointing out a commonly appreciated aspect of super-resolution imaging—the effective resolution is determined by a combination of the intrinsic imaging resolution and the size of the labels. Improvement in the effective resolution may be achieved by using direct immunofluorescence staining with dye-labeled primary antibodies or Fab fragments.

To demonstrate multicolor STORM imaging in cells, we simultaneously imaged microtubules and clathrin-coated pits (CCPs), cellular structures used for receptor-mediated endocytosis. Microtubules and clathrin were immunostained with primary antibodies and then activator-reporter-labeled secondary antibodies. The activator-reporter pairs used were Cy2-Alexa 647 for microtubules and Cy3-Alexa 647 for clathrin. The 457- and 532-nm lasers were used to selectively activate the two pairs. Cross talk between the two color channels due to false and

nonspecific activations was subtracted from the image after statistical analysis (26). Figure 4 shows the two-color STORM image presented at different scales. The intrinsic imaging resolution, as determined from the FWHM of pointlike clusters of localizations, was 30 ± 1 nm for each of the two color channels, slightly larger than the resolution determined for the single-color STORM images (fig. S6) (26). The green channel (457-nm activation) revealed filamentous structures as expected for microtubules, with a width quantitatively similar to that obtained from the single-color STORM image. The red channel revealed predominantly spherical structures, representing clathrin-coated pits and vesicles (Fig. 4 and fig. S7A) (26). In contrast to the STORM images, the conventional TIRF images of CCPs appeared as diffraction-limited spots without any discernable shape (fig. S7A). Side-by-side CCPs that were clearly resolved by STORM appeared as a single spot in the conventional image (fig. S7A). Many of the spherical CCPs appeared to have a doughnut shape with a higher density of localizations toward the periphery, which is consistent with the two-dimensional projection of a three-dimensional cage structure. Finally, the STORM image allowed us to measure the size distribution of CCPs (fig. S7B), which agrees quantitatively with the size distribution determined by electron microscopy (31). In summary, our two-color STORM images of cells clearly revealed ultrastructural information not discernable in conventional fluorescence images. This technique may be readily expanded to include more colors by using the photo-switchable activator-reporter pairs reported here, substantially enhancing our ability to visualize molecular interactions in cells and tissues. Further development of cell-delivery methods with molecular specificity will facilitate live cell imaging with these probes (14, 32).

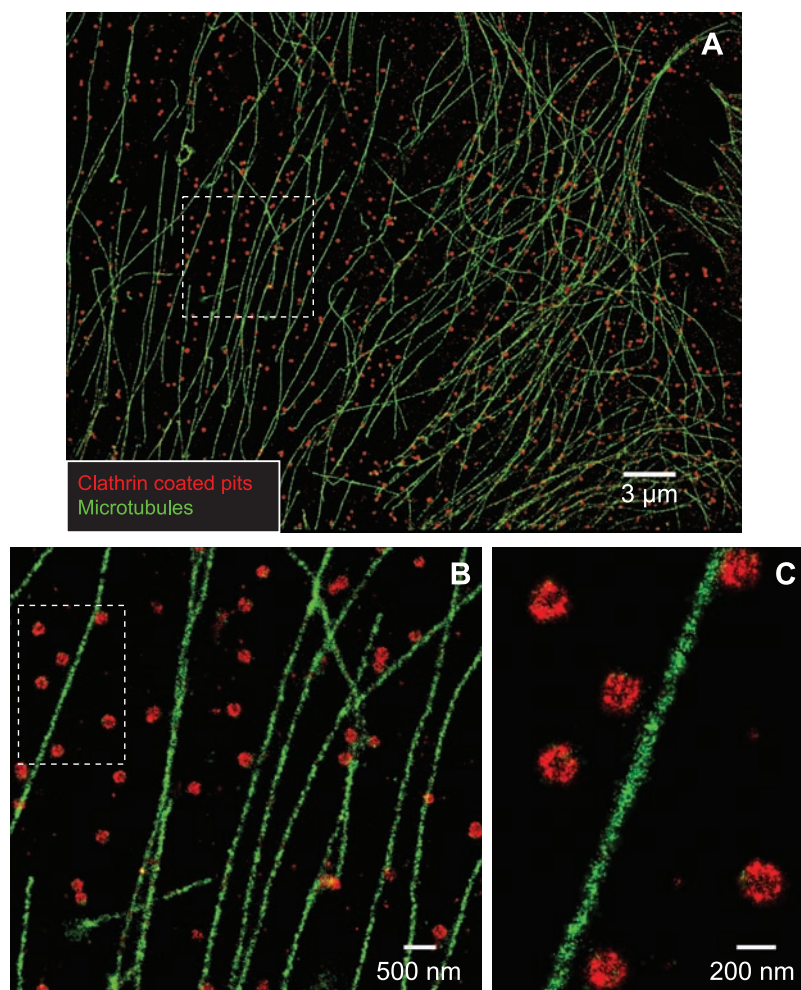


Fig. 4. Two-color STORM imaging of microtubules and CCPs in a mammalian cell. **(A)** STORM image of a large area of a BS-C-1 cell. The secondary antibodies used for microtubule staining were labeled with Cy2 and Alexa 647, and those for clathrin were labeled with Cy3 and Alexa 647. The 457- and 532-nm laser pulses were used to selectively activate the two pairs. Each localization was false colored according to the following code: green for 457-nm activation and red for 532-nm activation. **(B)** STORM image corresponding to the boxed region in **(A)** shown at a higher magnification. **(C)** Further magnified view of the boxed region in **(B)**.

References and Notes

1. L. Novotny, B. Hecht, *Principles of Nano-optics* (Cambridge Univ. Press, Cambridge, 2006).
2. S. W. Hell, *Science* **316**, 1153 (2007).
3. S. W. Hell, *Nat. Biotechnol.* **21**, 1347 (2003).
4. M. G. L. Gustafsson, *Proc. Natl. Acad. Sci. U.S.A.* **102**, 13081 (2005).
5. M. J. Rust, M. Bates, X. Zhuang, *Nat. Methods* **3**, 793 (2006).
6. E. Betzig *et al.*, *Science* **313**, 1642 (2006).
7. S. T. Hess, T. P. K. Girirajan, M. D. Mason, *Biophys. J.* **91**, 4258 (2006).
8. A. Ponti, M. Machacek, S. L. Gupton, C. M. Waterman-Storer, G. Danuser, *Science* **305**, 1782 (2004).
9. S. Y. Kim, Z. Gitai, A. Kinkhabwala, L. Shapiro, W. E. Moerner, *Proc. Natl. Acad. Sci. U.S.A.* **103**, 10929 (2006).
10. A. Sharonov, R. M. Hochstrasser, *Proc. Natl. Acad. Sci. U.S.A.* **103**, 18911 (2006).
11. L. Stryer, R. P. Haugland, *Proc. Natl. Acad. Sci. U.S.A.* **58**, 719 (1967).
12. T. Ha *et al.*, *Proc. Natl. Acad. Sci. U.S.A.* **93**, 6264 (1996).
13. T. Ha *et al.*, *Proc. Natl. Acad. Sci. U.S.A.* **96**, 9077 (1999).
14. B. N. G. Geppmans, S. R. Adams, M. H. Ellisman, R. Y. Tsien, *Science* **312**, 217 (2006).
15. G. Donnert *et al.*, *Biophys. J.* **92**, L67 (2007).
16. W. E. Moerner, M. Orrit, *Science* **283**, 1670 (1999).
17. R. E. Thompson, D. R. Larson, W. W. Webb, *Biophys. J.* **82**, 2775 (2002).

18. A. Yildiz *et al.*, *Science* **300**, 2061 (2003).
 19. M. P. Gordon, T. Ha, P. R. Selvin, *Proc. Natl. Acad. Sci. U.S.A.* **101**, 6462 (2004).
 20. X. Qu, D. Wu, L. Mets, N. F. Scherer, *Proc. Natl. Acad. Sci. U.S.A.* **101**, 11298 (2004).
 21. K. A. Lidke, B. Rieger, T. M. Jovin, R. Heintzmann, *Opt. Exp.* **13**, 7052 (2005).
 22. C. Kural *et al.*, *Science* **308**, 1469 (2005).
 23. X. L. Nan, P. A. Sims, P. Chen, X. S. Xie, *J. Phys. Chem. B* **109**, 24220 (2005).
 24. E. A. Abbondanzieri, W. J. Greenleaf, J. W. Shaevez, R. Landick, S. M. Block, *Nature* **438**, 460 (2005).
 25. S. Dumont *et al.*, *Nature* **439**, 105 (2006).
 26. See supporting material on Science Online.
27. M. Bates, T. R. Blosser, X. Zhuang, *Phys. Rev. Lett.* **94**, 108101 (2005).
 28. M. Heilemann, E. Margeat, R. Kasper, M. Sauer, P. Tinnefeld, *J. Am. Chem. Soc.* **127**, 3801 (2005).
 29. S. Hohng, C. Joo, T. Ha, *Biophys. J.* **87**, 1328 (2004).
 30. K. Weber, P. C. Rathke, M. Osborn, *Proc. Natl. Acad. Sci. U.S.A.* **75**, 1820 (1978).
 31. J. E. Heuser, R. G. W. Anderson, *J. Cell Biol.* **108**, 389 (1989).
 32. I. Chen, A. Y. Ting, *Curr. Opin. Biotechnol.* **16**, 35 (2005).
 33. We thank M. Rust for initial discussions of this work, W. Wang for help with analysis on dye-labeled antibodies, and S. Liu for providing some DNA constructs. This work

was supported in part by the National Institutes of Health (grant GM 068518) and a Packard Science and Engineering Fellowship (to X.Z.). X.Z. is a Howard Hughes Medical Institute Investigator.

Supporting Online Material

www.sciencemag.org/cgi/content/full/1146598/DC1
 Materials and Methods
 Figs. S1 to S7
 References

18 June 2007; accepted 3 August 2007
 Published online 16 August 2007;
 10.1126/science.1146598
 Include this information when citing this paper.

Widespread Lateral Gene Transfer from Intracellular Bacteria to Multicellular Eukaryotes

Julie C. Dunning Hotopp,^{1*}†‡ Michael E. Clark,^{2*} Deodoro C. S. G. Oliveira,² Jeremy M. Foster,³ Peter Fischer,⁴ Mónica C. Muñoz Torres,⁵ Jonathan D. Giebel,² Nikhil Kumar,^{1,†} Nadeeza Ishmael,^{1,†} Shiliang Wang,¹ Jessica Ingram,³ Rahul V. Nene,^{1,§} Jessica Shepard,^{1||} Jeffrey Tomkins,⁵ Stephen Richards,⁶ David J. Spiro,¹ Elodie Ghedin,^{1,7} Barton E. Slatko,³ Hervé Tettelin,^{1,†¶} John H. Werren^{2¶}

Although common among bacteria, lateral gene transfer—the movement of genes between distantly related organisms—is thought to occur only rarely between bacteria and multicellular eukaryotes. However, the presence of endosymbionts, such as *Wolbachia pipientis*, within some eukaryotic germlines may facilitate bacterial gene transfers to eukaryotic host genomes. We therefore examined host genomes for evidence of gene transfer events from *Wolbachia* bacteria to their hosts. We found and confirmed transfers into the genomes of four insect and four nematode species that range from nearly the entire *Wolbachia* genome (>1 megabase) to short (<500 base pairs) insertions. Potential *Wolbachia*-to-host transfers were also detected computationally in three additional sequenced insect genomes. We also show that some of these inserted *Wolbachia* genes are transcribed within eukaryotic cells lacking endosymbionts. Therefore, heritable lateral gene transfer occurs into eukaryotic hosts from their prokaryote symbionts, potentially providing a mechanism for acquisition of new genes and functions.

The transfer of DNA between diverse organisms, lateral gene transfer (LGT), facilitates the acquisition of novel gene functions. Among Eubacteria, LGT is involved

in the evolution of antibiotic resistance, pathogenicity, and metabolic pathways (1). Rare LGT events have also been identified between higher eukaryotes with segregated germ cells (2), demonstrating that even these organisms can acquire novel DNA. Although most described LGT events occur within a single domain of life, LGT has been described both between Eubacteria and Archaea (3) and between prokaryotes and phagotrophic unicellular eukaryotes (4, 5). However, few interdomain transfers involving higher multicellular eukaryotes have been found.

Wolbachia pipientis is a maternally inherited endosymbiont that infects a wide range of

arthropods, including at least 20% of insect species, as well as filarial nematodes (6). It is present in developing gametes (6) and so provides circumstances conducive for heritable transfer of bacterial genes to the eukaryotic hosts. *Wolbachia*-host transfer has been described in the bean beetle *Callosobruchus chinensis* (7) and in the filarial nematode *Onchocerca* spp. (8).

We have found *Wolbachia* inserts in the genomes of additional diverse invertebrate taxa, including fruit flies, wasps, and nematodes. A comparison of the published genome of the *Wolbachia* endosymbiont of *Drosophila melanogaster* (9) and assemblies of *Wolbachia* clone mates (10) from fruit fly whole-genome shotgun sequencing data revealed a large *Wolbachia* insert in the genome of the widespread tropical fruit fly *D. ananassae*. Numerous contiguous, overlapping, clone sequences (contigs) were found that harbored junctions between *Drosophila* retrotransposons and *Wolbachia* genes. The large number of these junctions and the deep sequencing coverage across the junctions indicated that these inserts were probably not due to chimeric libraries or assemblies. To validate these observations, we amplified five *Drosophila-Wolbachia* junctions with polymerase chain reaction (PCR) and verified the end sequences for three of them. Fluorescence in situ hybridization (FISH) of banded polytene chromosomes with fluorescein-labeled probes of two *Wolbachia* genes (11) revealed the presence of *Wolbachia* genes on the 2L chromosome of *D. ananassae* (Fig. 1).

We found that nearly the entire *Wolbachia* genome was transferred to the fly nuclear genome, as evidenced by the presence of PCR-amplified products from 44 of 45 physically distant *Wolbachia* genes in cured strains of *D. ananassae* Hawaii verified by microscopy to be lacking the endosymbiont after treatment with

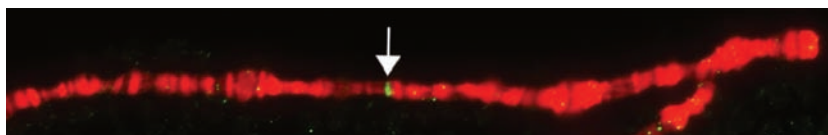


Fig. 1. Fluorescence microscopy evidence supporting *Wolbachia*/host LGT. DNA in the polytene chromosomes of *D. ananassae* were stained with propidium iodide (red), whereas a probe for the *Wolbachia* gene WD_0484 bound to a unique location (green, arrow) on chromosome 2L.

¹The Institute for Genomic Research, J. Craig Venter Institute, 9712 Medical Center Drive, Rockville, MD 20850, USA. ²Department of Biology, University of Rochester, Rochester, NY 14627, USA. ³Molecular Parasitology Division, New England Biolabs Incorporated, 240 County Road, Ipswich, MA 01938, USA. ⁴Department of Internal Medicine, Infectious Diseases Division, Washington University School of Medicine, St. Louis, MO 63110, USA. ⁵Clemson University Genomics Institute, 304 BRC, 51 New Cherry Street, Clemson, SC 29634, USA. ⁶Human Genome Sequencing Center, Baylor College of Medicine, Houston, TX 77030, USA. ⁷Division of Infectious Diseases, University of Pittsburgh School of Medicine, Pittsburgh, PA 15261, USA.

*These authors contributed equally to this work.

†To whom correspondence should be addressed. E-mail: jhotopp@som.umaryland.edu

‡Present address: Institute for Genome Sciences, University of Maryland School of Medicine, Health Sciences Facility II, Room 5-445, 20 Penn Street, Baltimore, MD 21201, USA.

§Present address: Brown University, Providence, RI 02912, USA.

|| Present address: Pace University, New York, NY 10038, USA.

¶These authors contributed equally to this work.